

The MUSE Beamline Calorimeter

W. Lin,^{1,*} T. Rostomyan,² R. Gilman,¹ S. Strauch,³ C. Meier,⁴ C. Nestler,^{2,5} M. Ali,⁶ H. Atac,⁷ J. C. Bernauer,^{8,9} W. J. Briscoe,¹⁰ A. Christopher Ndukwe,¹¹ E. W. Cline,^{8,12} K. Deiters,² S. Dogra,¹ E. J. Downie,¹⁰ Z. Duan,¹ I. P. Fernando,^{11,†} A. Flannery,^{3,‡} D. Ghosal,^{4,§} A. Golossanov,¹⁰ J. Guo,¹ N. S. Ifat,⁷ Y. Ilieva,³ M. Kohl,¹¹ I. Lavruchin,^{10,13} L. Li,^{3,¶} W. Lorenzon,¹³ P. Mohanmurthy,^{14,**} S. J. Nazeer,¹¹ M. Nicol,³ T. Patel,¹¹ A. Prosnjakov,¹⁵ R. D. Ransome,¹ R. Ratvasky,¹⁰ H. Reid,¹³ P. E. Reimer,¹⁶ R. Richards,¹¹ G. Ron,¹⁵ O. M. Ruimi,^{15,17} K. Salamone,⁸ N. Sparveris,⁷ N. Wuerfel,^{13,12} and D. A. Yaari¹⁵

¹*Department of Physics and Astronomy, Rutgers,*

The State University of New Jersey, Piscataway, NJ 08855, USA

²*Laboratory for Particle Physics, PSI Center for Neutron and Muon Sciences, 5232 Villigen, CH*

³*Department of Physics and Astronomy, University of South Carolina, Columbia, SC 29208, USA*

⁴*Department of Physics, University of Basel, 4056 Basel, CH*

⁵*Institute for Particle Physics and Astrophysics, ETH Zürich, 8092 Zürich, CH*

⁶*Department of Physics, New Mexico State University, Las Cruces, NM 88003, USA*

⁷*Department of Physics, Temple University, Philadelphia, PA 19122, USA*

⁸*Center for Frontiers in Nuclear Science, Stony Brook University, Stony Brook, NY 11794, USA*

⁹*Department of Physics and Astronomy, Stony Brook University, Stony Brook, NY 11794, USA*

¹⁰*Department of Physics, The George Washington University, Washington, DC 20052, USA*

¹¹*Department of Physics, Hampton University, Hampton, VA 23668, USA*

¹²*Laboratory for Nuclear Science, Massachusetts Institute of Technology, Cambridge, MA 02139, USA*

¹³*Randall Laboratory of Physics, University of Michigan, Ann Arbor, MI 48109, USA*

¹⁴*Department of Physics, University of Chicago, Chicago, IL 60615, USA*

¹⁵*Racah Institute of Physics, Hebrew University of Jerusalem, Jerusalem 91904, IL*

¹⁶*Physics Division, Argonne National Laboratory, Lemont, IL 60439, USA*

¹⁷*Helmholtz Institute, Johannes Gutenberg University Mainz, 55128 Mainz, DE*

The MUon Scattering Experiment (MUSE) was motivated by the proton radius puzzle arising from the discrepancy between muonic hydrogen spectroscopy and electron-proton measurements. The MUSE physics goals also include testing lepton universality, precisely measuring two-photon exchange contribution, and testing radiative corrections. MUSE addresses these physics goals through simultaneous measurement of high precision cross sections for electron-proton and muon-proton scattering using a mixed-species beam. The experiment will run at both positive and negative beam polarities. Measuring precise cross sections requires understanding both the incident beam energy and the radiative corrections. For this purpose, a lead-glass calorimeter was installed at the end of the beam line in the MUSE detector system. In this article we discuss the detector specifications, calibration and performance. We demonstrate that the detector performance is well reproduced by simulation, and meets experimental requirements.

I. INTRODUCTION

The Proton Radius Puzzle was the observation of a significantly smaller proton charge radius determined in muonic hydrogen spectroscopy than had been determined from atomic hydrogen spectroscopy and electron proton scattering [1, 2]. This observation led to strong interest in the proton radius and related physics of potential

new forces, lepton universality, and radiative corrections, including two-photon exchange and polarizability. Possible explanations for the puzzle generally fall into the categories of new forces, novel aspects of conventional physics, or issues in experimental extractions of the radius. While there are new electronic measurements of the radius in agreement with the muonic spectroscopy result, the lack of overall agreement among the new results suggests that there are ongoing experimental issues in determining the radius [3].

The MUSE experiment, motivated by a lack of high-precision muon-scattering data that addresses these physics issues, is working towards a sub-percent level, high-precision experiment that simultaneously measures elastic electron-proton scattering and muon-proton scattering. MUSE is located at the Paul Scherrer Institute in Villigen, Switzerland. The High-Intensity Proton Accelerator facility uses a cyclotron to produce an approximately 2 mA, 590 MeV proton beam. The beam passes through the graphite-wheel M target to produce electrons, muons and pions that are transported by the

* Current: Center for Frontiers in Nuclear Science & Department of Physics and Astronomy, Stony Brook University, Stony Brook, NY 11794, USA

† Current: Department of Physics, University of Virginia, Charlottesville, VA 22904, USA

‡ Current: Department of Physics, Hampton University, Hampton, VA 23668, USA

§ Current: Cockcroft Institute, Sci-Tech Daresbury, University of Liverpool, Warrington WA4 4AD, UK

¶ Current: ASML, 80 W Tasman Dr, San Jose, CA 95134, USA

** Current: Laboratory for Nuclear Science, Massachusetts Institute of Technology, Cambridge, MA 02139, USA

PiM1 channel to MUSE. MUSE has run at three momentum settings, of 115 MeV/c, 160 MeV/c and 210 MeV/c, at selectable positive or negative beam polarity [4].

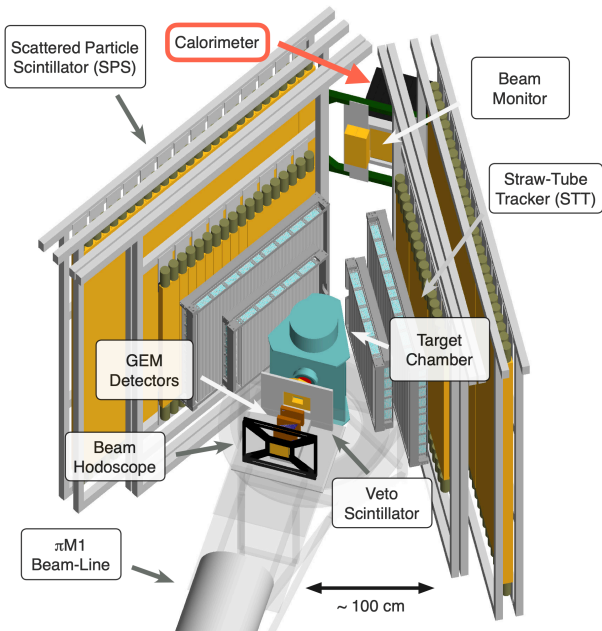


FIG. 1: Geant4 drawing of the MUSE system, showing the calorimeter at the downstream (upper right) end of the detector system.

MUSE comprises beamline and scattering detectors. Figure 1 is a drawing of the full detector setup. The first two detectors in the beam are a two-plane plastic scintillator Beam Hodoscope (BH) [5] and a four-plane Gas Electron Multiplier (GEM) detector. These two detectors provide incoming particle timing, species identification, and tracking. Downstream of the GEM detector are the veto scintillator detector (VETO) and the trapezoidal target chamber [6]. The annular VETO detector rejects events with beam particle trajectories that hit the target chamber walls, such as decays in flight and beam halo. On both sides of the target chamber, the Straw-Tube Tracker (STT) and Scattered Particle Scintillator (SPS) are responsible for scattered event tracking and timing. Downstream of the target chamber the Beam Monitor (BM) and calorimeter (CALO) help monitor the beam, measure its energy, and identify events with high energy forward-going photons.

Extracting precise Born cross sections and the proton radius from the experimental scattering cross sections requires radiative corrections to account for the contribution of higher-order processes to the scattering cross section. The leading-order correction with additional particles in the final state is the Bremsstrahlung correction, in which the charged leptons or protons emit real photons when accelerated. This correction generates a radiative tail, a continuous distribution in momentum for the nominally two-body elastic scattering $ep \rightarrow ep$ reaction. This

correction is most significant for electrons, as it is suppressed for muons and pions due to their higher mass.

Most electron-scattering experiments use magnetic spectrometers, and the measured spectrum and limited momentum acceptance of the experiments allow the Bremsstrahlung correction to be calculated with good precision. MUSE, however, runs with a large solid angle, non-magnetic spectrometer. As a result, MUSE measurements integrate over a wide range of outgoing electron momenta, including most of the radiative tail, to determine the cross section. The experimental uncertainty is sensitive to the limits of integration over the radiative tail, determined by detector thresholds on particle energy loss. MUSE employs two strategies that allow radiative corrections to be studied with the experimental data, with the goal of limiting the associated uncertainty from these corrections. One strategy is to use a low detector hardware threshold along with a software energy loss cut in the analysis. This procedure allows the cut and its uncertainties to be checked with simulations. A second strategy is to suppress the Bremsstrahlung correction by removing events from the analysis with high-energy, forward-going photons. This limits the initial-state radiation, largely removing the low-energy tail of the momentum distribution, due to the dominance of the initial-state over the final-state Bremsstrahlung correction – the initial-state radiation moves the vertex to lower Q^2 and thus higher cross section.

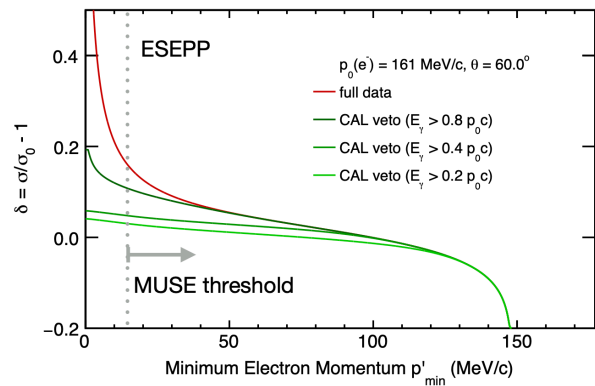


FIG. 2: Radiative corrections for ep scattering as a function of the minimum electron momentum at one MUSE kinematic setting, calculated using the ESEPP event generator [7]. The radiative correction factor δ indicates the difference between the experimental and Born cross sections: $\sigma/\sigma_0 = 1 + \delta$. See Ref. [8] for details.

Removing events with high-energy photons is done with the lead-glass calorimeter installed at the most downstream position of the experiment. Figure 2, reproduced from Ref. [8], shows an example of the dependence of the radiative correction on the minimum electron momentum in the integration. The red curve represents the radiative correction for ep scattering when there is no

suppression of high-energy photons. The green curves are the radiative correction including calorimeter energy cuts in the data analysis. With the photon energy cuts, the corrections are less sensitive to the electron momentum threshold in the MUSE threshold region, where integration begins. Thus, the sensitivity and the resulting uncertainties are reduced. In particular, with a photon energy cut of greater than 40% of the beam momentum, the correction is small and nearly linear in the region of the cut, limiting this important experimental systematic correction and uncertainty [8]. The variation of cross section with these radiative corrections cuts is a strong test for MUSE that can demonstrate the quality of the applied radiative corrections, and that they are well understood.

The MUSE calorimeter specifications were developed based on Geant4 simulations with ESEPP radiative corrections [7] shown in Fig. 2. The cross section can be increased or decreased by offsets in the calorimeter light output calibration and by detector resolution, depending on the slope of the flux and the variation in resolution near threshold. With the goal of limiting changes in the absolute cross section from these resolution and offsets to the 0.1% level, we observed in the simulation that the calorimeter light output scale needed to be determined to approximately 2 MeV in the cut region, and corrections could be performed at an acceptable level for a resolution near threshold of approximately $5\%/\sqrt{E}$, with E in GeV.

In the following sections, we discuss the hardware details, calibration procedures and performance of the calorimeter. We show that detector simulations agree well with the experimental data.

II. DETECTOR DESCRIPTION

The calorimeter detector consists of an 8×8 array of SF5 lead-glass crystals¹, on loan from the A2 experiment @ MAMI [9]. The radiation length and Molière radius of lead-glass are 1.265 cm and 2.578 cm, respectively [10]. Figure 3 shows a schematic drawing of a calorimeter crystal and the associated photomultiplier. The crystals are 24 radiation lengths long along the beam direction. Each lead-glass crystal is individually wrapped with aluminized Mylar foil and black shrink tubing for optical isolation. The detector signals are read out by Hamamatsu R1355 photo-multiplier tubes (PMTs), which produce a negative anode signal.

When particles directly hit the center of a crystal, that crystal absorbs most of the particle's kinetic energy, with a small fraction of the energy spreading to neighboring crystals. However, particles can hit edges and corners of

the crystals, depositing significant energy in the neighboring crystals. Hence, most of the energy of an incoming particle is easily captured by summing the energy of the crystal with maximum energy with the energies of the 8 surrounding neighbors. The energy response and analysis will be discussed more in Sec. IV.

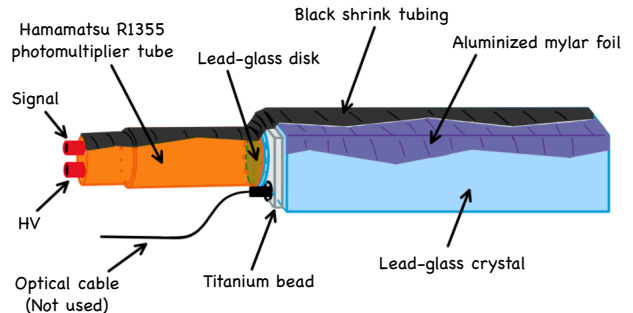


FIG. 3: Schematic drawing of a calorimeter crystal. Each crystal is $4 \text{ cm} \times 4 \text{ cm} \times 30 \text{ cm}$ in dimension. The PMT shown to the left is at the downstream end of the crystal [9, 11].

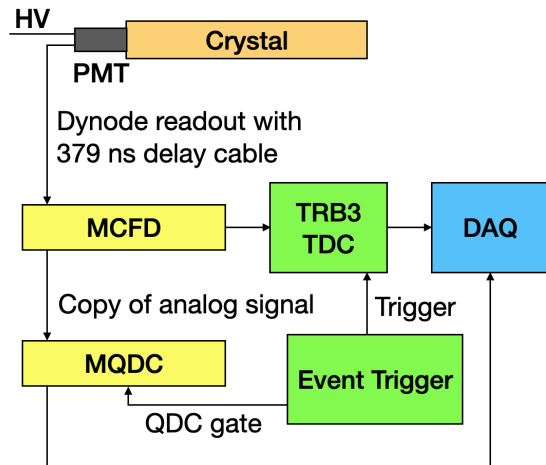


FIG. 4: Schematic drawing of the calorimeter readout.

Figure 4 shows a schematic drawing of the readout electronics. The signals propagate through delay lines before entering the Mesytec MCFD-16 constant fraction discriminators (CFDs) [12]. Figure 5 shows typical crystal signals in an oscilloscope, after the delay, before being input to the CFDs. Data are for a 210 MeV/c negative polarity beam, comprised of approximately 30% e 's, 5% μ 's, and 65% π 's, with e 's (π 's) generating the largest (smallest) signals. The CFDs generate logical timing signals that are digitized by TRB3 TDCs [13]. The CFDs also send copies of the analog signals to Mesytec MQDC-32 Charge to Digital Converters (QDCs) [14] for integration with 12-bit precision. While the QDC information is sufficient to determine light output in the detector for

¹ Each crystal has optical fibers that can input calibration test signals. These unused optical cables were sealed into a light-tight box located on top of the crystal array.

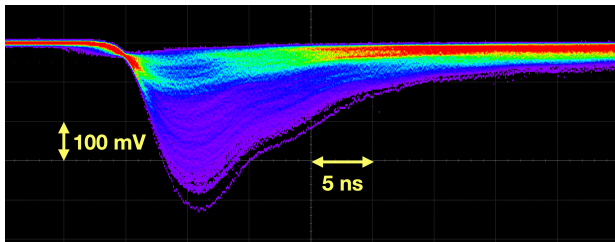


FIG. 5: Calorimeter signals from a mixed, negatively charged particle beam at 210 MeV/c, after the 379 ns long delay.

each event, the few MHz beam rate leads to light output from randomly coincident beam particles. The TDC information helps to distinguish in-time clusters from a scattering event from clusters from randomly coincident beam particles that are also read out in the same event.



FIG. 6: Photographs of the calorimeter from three perspectives. **Top Left:** Side view from beam left. **Bottom Left:** Looking downstream towards the upstream face of the calorimeter. **Right:** Looking upstream at the full detector including the light-tight box on top of the crystals and the PMTs.

Figure 6 shows pictures of the calorimeter detector viewed from different directions. The front face of the calorimeter is located 138.5 cm from the center of the target. The detector covers an area of about 33 cm by 33 cm, or an angular range of about $\pm 6.8^\circ$ in horizontal and vertical directions, which is sufficient to capture most of the forward-going photons. Figure 7 shows the simulated photon distribution at the front face of the calorimeter before and after the calorimeter cuts. With this calorimeter design, most of the high-energy-photon

events will be removed in the analysis, while the the lower energy photon events will be retained.

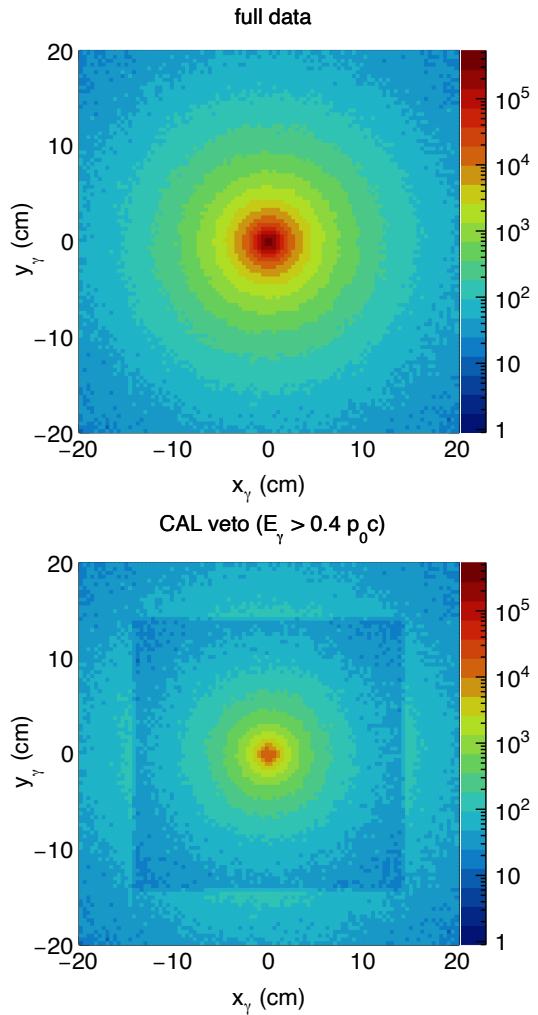


FIG. 7: Simulated photon distribution at the front face of the calorimeter. **Top:** All photons. **Bottom:** Distribution of photons after applying a calorimeter energy cut. The central area with less counts compared to the top plot reflects the size of the detector.

III. CALIBRATION PROCEDURES

The goal of the calibration procedure is to convert the signal sizes in each detector channel, which are proportional to the light generated by electrons in the crystals, to an energy, so that the incident electron energies can be determined. The calibration requires both gain matching the calorimeter crystals and determining the light output scale. Gain is the proportionality between the output QDC values and the particle signal size in the detector. We calibrate the gain for each channel to ensure the detector light output derived is consistent for all channels. It is convenient to use both cosmic rays

and beam particles for this purpose. Cosmic rays are always available and illuminate the calorimeter crystals more uniformly than does the beam. However, light from cosmic rays is not collected with the same efficiency as for beam particles due to the different trajectories of the particles, so determining an absolute light output scale is more straightforward with beam particles of known energy. We focus on the response of the calorimeter to electrons in the beam, which generate similar signals in the calorimeter to photons of the same energy. Thus, we initially gain match with cosmics, and then we calibrate the absolute energy scale with beam.

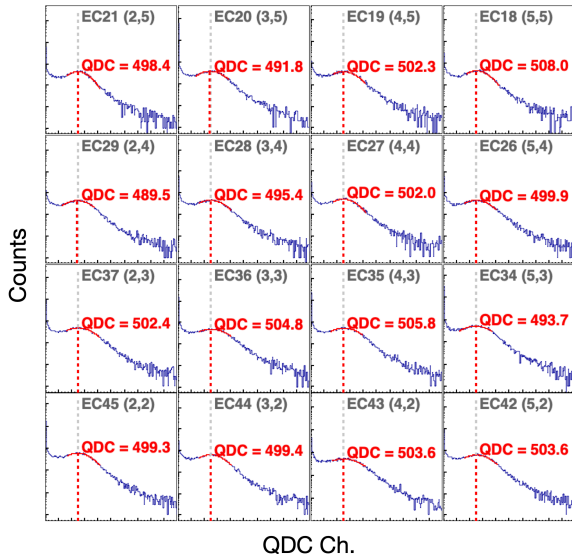


FIG. 8: Semi-log graphs of QDC spectra of the central 16 crystals after gain matching using cosmics. QDC peaks are aligned to channel 500 with software calibrations.

The gain is calibrated in two steps. First, a hardware gain match adjusts PMT HV. Second, the QDC response of each channel is fine tuned in software. During the hardware gain matching, we adjust PMT high voltages to approximately match the positions of the peaks in the QDC spectra of each crystal. The Hamamatsu R1355 PMT has 10 dynode stages. The relationship between applied high voltage and gain was found to be

$$\frac{\text{gain}_{\text{new}}}{\text{gain}_{\text{old}}} = \left(\frac{V_{\text{old}}}{V_{\text{new}}} \right)^k, \quad (1)$$

where k was determined empirically to be approximately 8, with some variation between crystals. Following this relation, the high voltage applied to each channel of the detector is adjusted iteratively until the QDC peak positions of the cosmic events for each crystal are roughly matched at around QDC channel 500. This setting optimizes the calorimeter performance while keeping the QDC spectra from overflowing at higher beam momentum settings. At the highest beam momentum setting

for data, 210 MeV/c, the QDC peaks are at about channel 3100, with a long tail reaching to channel 3840, near the end of the 12-bit QDC range. After the hardware gain match, in the software gain matching step, we fine tune the gain match by fitting the QDC peak of the cosmic signal for each bar, determining the factor needed to scale the peak position to the common QDC channel of 500. An example of the QDC spectra of the central crystals after the gain matching calibration is shown in Fig. 8.

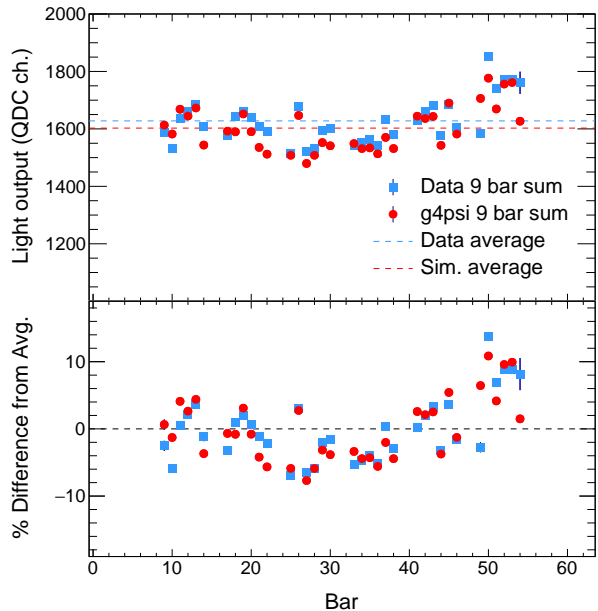


FIG. 9: Data for position of the calorimeter QDC peak in units of QDC channels vs. the channel number of the crystal with the maximum light output, and the percent difference of that peak position from the average of the 9 bar sums, at 110 MeV/c. The crystal numbers increment across the rows of the calorimeter crystals, from the top row to the bottom.

Finally, to check the uniformity of the gain matching, the cluster energies are determined as a function of position in the calorimeter. Figure 9 shows the result of this study, where the cluster light output sum vs. central bar location for 110 MeV/c beam data are plotted. From the figures, the average light output of clusters with a 9-bar sum is roughly the same independent of their position. To better understand the distribution, we compare the data to simulation. The simulation reproduces the behavior of the light output peak vs. crystal position with maximum light output. More details about the calorimeter simulation and data digitization will be discussed in later sections.

IV. DETECTOR PERFORMANCE

For each event, the sum of light output in the calorimeter is determined. First, the crystal with the highest QDC value is found. Second, the light output of that crystal and the eight surrounding neighbors are summed. Third, a search is performed for additional clusters away from the first cluster found. TDC information is checked for each cluster to determine if it is in-time, so that energy cuts should be applied.

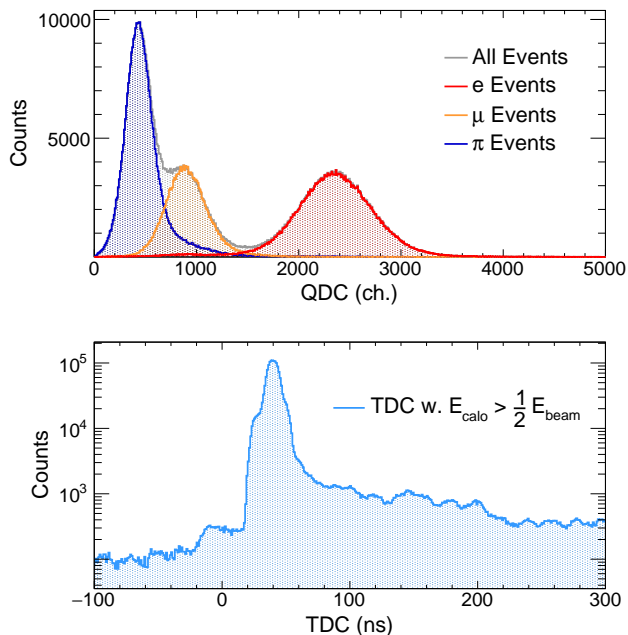


FIG. 10: **Top:** Distribution of calorimeter light output 9-bar sums for beam particle events taken at momentum of 160 MeV/c. The distributions from different particle types are normalized to the same peak height as the distribution for all events. **Bottom:** TDC times relative to the event trigger for events with light output greater than half of the beam energy. The in-time peak is at ≈ 40 ns.

Figure 10 shows the 9-bar QDC sum for the calorimeter at 160 MeV/c beam momentum. Data were taken with a beam particle trigger at approximately 180 kHz beam rate, leading to an accidental coincidence rate within the 200-ns QDC gate of approximately 4%. Incident particle species are identified using timing information from the BH with respect to the accelerator RF [15]. The bottom of Fig. 10 shows the TDC distribution of the calorimeter for events with light output greater than half of the beam energy. The in-time peak at approximately 40 ns is for particles triggering the system. The small background at earlier times reflects particles that did not trigger the DAQ system, as it was still processing a previous event. In contrast, particles arriving after the triggering particle will generate signals, unless they overlap the triggering

particle by being in the same calorimeter crystals within the 25-ns TDC dead time. Hence, the random coincident background is higher after the trigger peak than before the trigger peak. The 19.75-ns beam RF structure leads to time structure in the random background events. It is washed out by the multiple particle types at different phases of the RF convoluted with 10-ns FPGA clocks in the trigger.

To distinguish the photon events from the leptons and pions, the BM detector in front of the calorimeter is used. Photons are not expected to leave a signal in the thin scintillators of the BM, while electrons, muons and pions will deposit energy in the detector. In the following sections, the calorimeter detector performance will be shown using electrons, which generate similar signals in the calorimeter to photons of the same energy.

A. Energy Response

Beam data were used to study and calibrate the calorimeter absolute light output response as shown in Fig. 11. The PiM1 beam line is designed to operate at momenta above about 100 MeV/c [4]. To map out the detector response in a wide range of energy, data were taken at beam momenta from 20 MeV/c to 230 MeV/c, and simulations were used to estimate the energy of the particles entering the calorimeter. The momentum scan result shows that the light output in the calorimeter as a function of the beam energy is very close to linear. The data are fit with a linear function to check linearity and to determine parameters to be used in the simulation to model the detector light output. The light output resolution of the detector is fit with $\frac{\sigma}{E} = \sqrt{\frac{a^2}{E} + b^2 + \frac{c^2}{E^2}}$, which is commonly used to describe the resolution of calorimeters [16]. In this fit, a is the stochastic term that is governed by the electromagnetic shower fluctuations in the material, b is the systematic term that reflects the uniformity of the detector and how well the detector is calibrated, and c is the noise term from electronic readout when measuring the energies. Typical light output resolutions for lead glass calorimeters are about $5\%/\sqrt{E/\text{GeV}}$ [16]. For the MUSE calorimeter, the parameters from the fit in Fig. 11 indicates that the resolution from the stochastic term is about $5.17\%/\sqrt{E/\text{GeV}}$. About 6.22% resolution arises from the b calibration term, while less than 1% is from the electronics.

B. Detector Timing

Light output in the calorimeter from randomly coincident beam particles can be identified by two techniques. The BM hodoscope immediately upstream of the calorimeter localizes incoming charged particles at the cm level in position and at the 100 ps level in time. The light

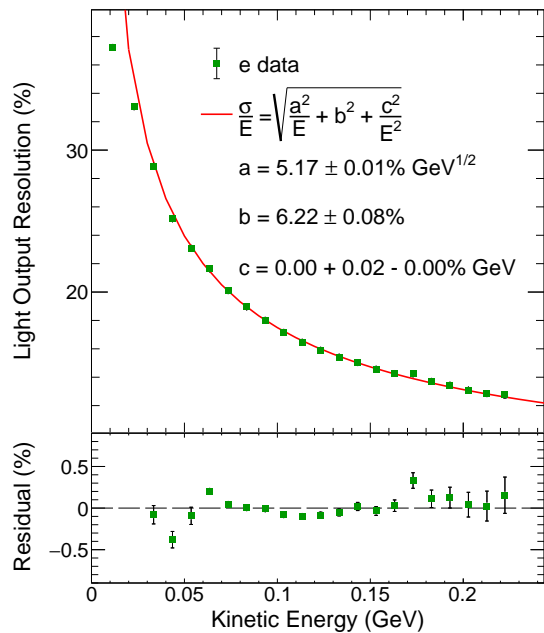
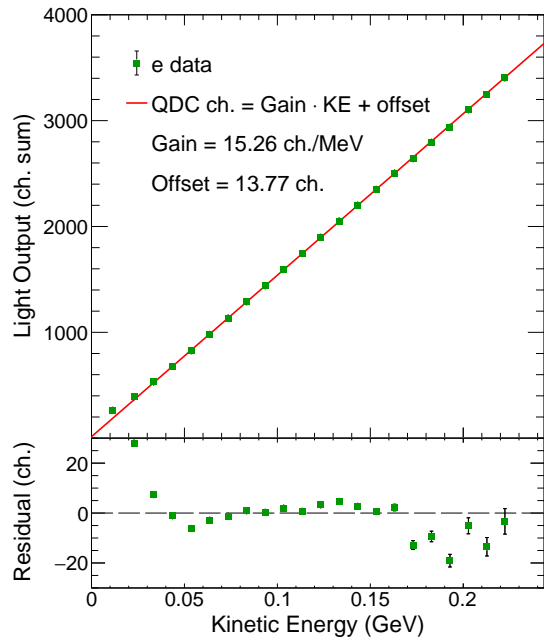


FIG. 11: Energy scan results for positrons. **Top:** Light output vs. beam momentum. **Bottom:** Resolution vs. beam momentum. Residuals of the fits are shown at the bottom of each plot with at most two energy outliers off the scale.

output from these beam particles is known from the beam momentum. The MUSE calorimeter also reads out timing information for the calorimeter crystals to help distinguish multiple hits in the detector, from both charged particles and photons. Figure 12 shows the example of calorimeter timing for a central crystal at 160 MeV/c.

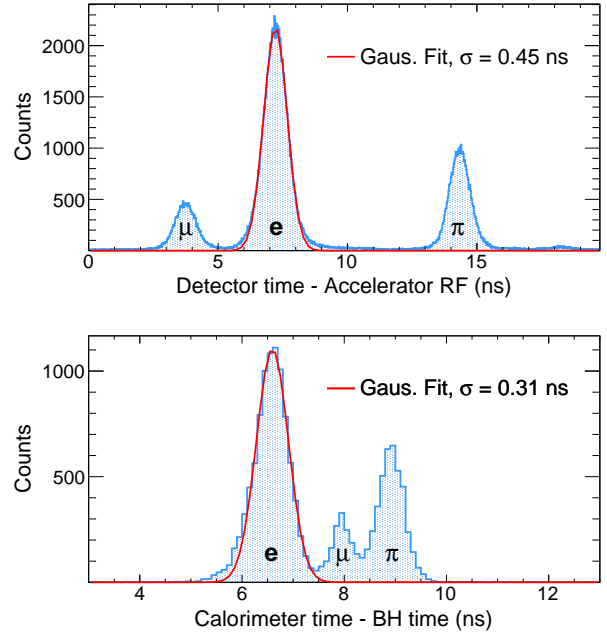


FIG. 12: TDC times of a central calorimeter crystal at 160 MeV/c, before walk corrections. **Top:** RF time, the difference in time between the calorimeter signal and the accelerator RF signal. **Bottom:** Time difference between calorimeter and BH signals, offset by an arbitrary constant. Walk corrections have not been applied to the calorimeter timing.

The top plot shows the detector time relative to the accelerator RF (modulo the RF period). The distribution shows three distinct peaks for the three particle types in the beam. The bottom plot shows time of flight from the beam hodoscope to the calorimeter, over a flight path of approximately 2.2 m. The electron, muon and pion peaks are also observed. The separation of the timing peaks of different particles shown in Fig. 12 makes clear that the timing information is sufficient to detect, localize and identify randomly coincident beam particles, other than those in the same crystals within the electronic dead times, approximately 25 ns.

C. Simulation

The MUSE setup is simulated with Geant4. The simulation records hits and saves the events to a ROOT output tree. The simulated data is digitized and run through the same analysis as experimental data to allow a direct comparison of simulation to data. For the calorimeter, the simulation records Cherenkov light production in the crystals. There are two modes of simulation that can be selected: a fast simulation that integrates a light yield over the path in the crystal for $\beta > c/n$, and a more detailed simulation that creates optical photons at each reaction step and tracks those that reach the PMTs. Cur-

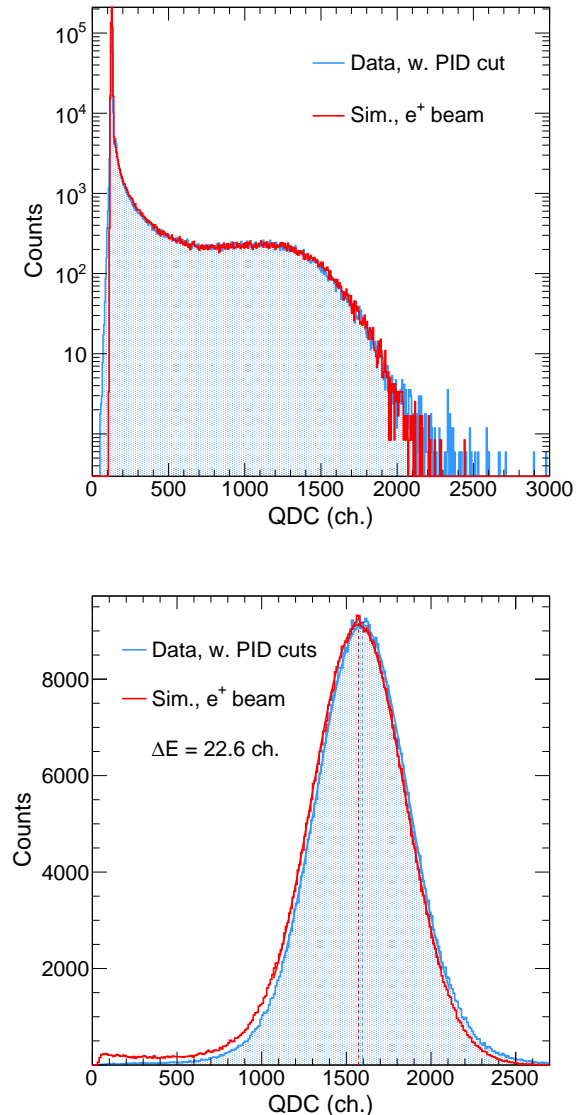


FIG. 13: **Top:** Positron QDC spectra of data and simulation for a central crystal. **Bottom:** Positron light output 9-bar sum for data and simulation at +110 MeV/c.

rent indications are that it is not necessary to run the simulation in the much more computationally intensive photon-counting mode. Here, we will show the preliminary calorimeter simulation result using the fast simulation mode. In this mode of the simulation, we calculate the light output by estimating the number of photons produced by the Cherenkov radiation. Since the number of photons emitted by incident particles is proportional to $(1 - \frac{1}{n^2\beta^2})$, for each reaction step in the simulation, we can find the relation for the number of photo-electrons

read out in an event by the calorimeter as

$$\delta N = f \times \delta l \times \left(1 - \frac{1}{n^2\beta^2}\right), \quad (2)$$

where δl is the step length, n is the index of refraction, and f is scaling factor tuned to match the simulation to data. Integrating δN for all the steps in the crystal determines the total number of photo-electrons generated by particles in the crystal.

The digitization converts the simulated light output of the calorimeter crystal to detector QDC channels. The pedestal of each QDC spectrum is modeled with a Gaussian distribution with the same width as the data, which is found during the calibration. If the bar has energy deposited in it, the energy is multiplied by a factor to more precisely model the gain of the detector and then randomized with a Gaussian, where the width of the distribution is equal to

$$\sigma = E \sqrt{\frac{\alpha^2}{E} + \frac{\gamma^2}{E^2}}. \quad (3)$$

The values of parameter α ($\approx 4.46\%$ GeV^{1/2}) and γ ($\approx 0.066\%$ GeV) are similar to the parameter a and c in the resolution fit of the light output scan calibration shown in Fig. 11. Because the simulation has some resolution effects already when calculating the light output for each reaction steps in the crystal, the additional resolution needed at the digitization is smaller than the fit values from the data.

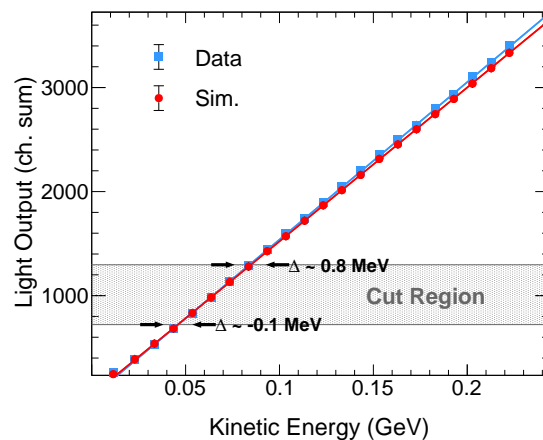


FIG. 14: Comparison between data and simulation for calorimeter light output sum (in units of QDC channels) for electrons vs. beam momentum. Linear fits are performed to compare differences at different beam energies. The arrows show the differences between data and simulation for the QDC values for the default radiative corrections cuts for 115 MeV/c (bottom of the gray band) and 210 MeV/c (top of the gray band).

The digitized, simulated data are processed through the same analysis as the experimental data. Figure 13

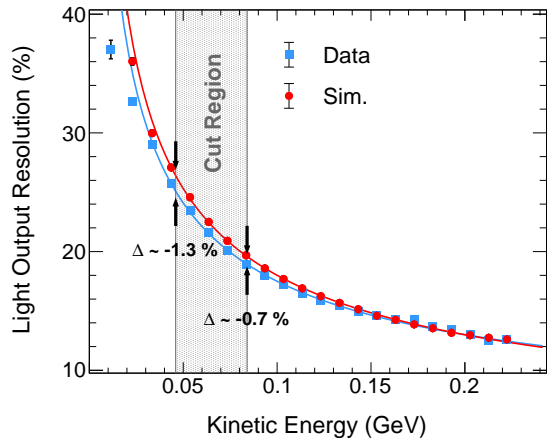


FIG. 15: Comparison between data and simulation for calorimeter light output resolution for electrons vs. beam momentum. Resolution fits as discussed in Sec. IV A are performed to compare differences at different beam energies. The arrows show the differences between data and simulation for the default radiative corrections cuts for 115 MeV/c (left edge of the gray band) and 210 MeV/c (right edge of the gray band).

compares data and simulation for the spectrum of a single crystal and for the 9-bar light output sum from the calorimeter. The data and simulation agree well, with a small mismatch at the mean value. This difference is due to a mismatch in the energy to QDC conversion between data and simulation for some channels, along with small differences in the air gap between bars.

Figures 14 and 15 compare the 9-bar-sum light output response and resolution of data and simulation at different momentum settings. Both data and simulation show similar linear relationships in the light output response, and similar light output resolution. While there is some disagreement at higher momenta, in the region where event cuts will be applied for radiative corrections (40% of the beam energy), the differences are small and the agreement is better than our 2-MeV requirement. Note that the energy to QDC channel conversion presented here is based on a calibration at one momentum setting, 110 MeV/c – no tuning was done to adjust the light output response of the simulation to match the data.

V. RECONSTRUCTED PHOTONS

Figure 16 presents an example of the light output distribution of the reconstructed photons in the calorimeter for data and preliminary simulation. The default radiative correction cut at $E_\gamma < 0.4p_0c$, where p_0 is the beam electron momentum, is indicated by the dashed line. The two distributions are similar in shape for the high energy photon events, with simulation being slightly nar-

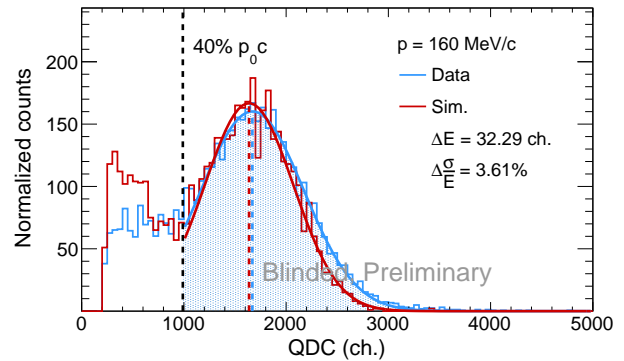


FIG. 16: Reconstructed photon QDC spectra of data and simulation for 160 MeV/c electron scattering with liquid hydrogen target. Black dashed line on the left indicates the default radiative correction cut for this momentum setting. Blue and red dashed lines indicate the mean position of the Gaussian fit of the high energy photon peaks.

rower in width. The slight mismatch in resolution is expected as the simulation is at a preliminary stage with the calorimeter energy calibration based on one momentum setting only, and as the scattered-particle scintillator energy cuts have not been precisely matched in simulation and in data. The difference in the lower energy events is due to the difference in threshold setting between data and simulation. Both data and simulation show a prominent peak from the high-energy photons emitted by some scattering electrons, as expected. The radiative correction cut will remove these events, reducing the experiment's sensitivity to radiative corrections. The agreement between the calibrated data and simulation indicates that the calorimeter performance is sufficient to obtain the needed experimental uncertainties. Further tuning in the simulation calibration, including calibration using data taken at multiple energies and studying possible time dependence of the calorimeter response will improve the agreement to be better than requirements.

VI. SUMMARY

In order to have radiative corrections under control for the MUSE scattering experiment, a lead-glass calorimeter detector was built to capture high-energy photons from initial-state radiation. Studies show that the detector has an light output response and resolution sufficient to identify and remove these events. The understanding of the detector behavior is demonstrated by comparing calibration measurements to simulation. With the calorimeter, MUSE will be able to test and control radiative corrections.

VII. ACKNOWLEDGEMENTS

This work is supported by the National Science Foundation, grants NSF PHY-1913653, PHY-2209348, PHY-2110229, PHY-2111050, PHY-2310026, PHY-2113436, PHY-1812402, PHY-1505934, PHY-2012114, PHY-2012940, PHY-2310026, PHY-10011349, and HRD-1649909, the U.S. Department of Energy Office of Science, office of Nuclear Physics under contract nos. DE-SC0016577, DE-SC0019768, DE-AC02-06CH11357, DE-SC0012589, and DE-SC0014448, the US-Israel Binational

Science Foundation (BSF) Grant 2020796, Schweizerischer Nationalfonds (SNF) 200020-156983, 132799, 121781, 117601, and the Paul Scherrer Institute. M. Kohl has been jointly supported by Jefferson Lab.

We are deeply grateful to the Mainz A2 collaboration for lending us the lead-glass crystals, which were essential in constructing the calorimeter. We thank the Paul Scherrer Institut for providing the necessary facilities, beam and resources for our research. We acknowledge PSI “Hallendienst” for their help in reinforcing the MUSE platform for the calorimeter.

-
- [1] R. Pohl, A. Antognini, F. Nez, F. D. Amaro, F. Biraben, J. M. Cardoso, D. S. Covita, A. Dax, S. Dhawan, L. M. Fernandes, and et al., The size of the proton, *Nature* **466**, 213–216 (2010).
- [2] A. Antognini, F. Nez, K. Schuhmann, *et al.*, Proton structure from the measurement of 2s-2p transition frequencies of muonic hydrogen, *Science* **339**, 417 (2013), <https://www.science.org/doi/pdf/10.1126/science.1230016>.
- [3] Bernauer, Jan C., The proton radius puzzle – 9 years later, *EPJ Web Conf.* **234**, 01001 (2020).
- [4] E. Cline, W. Lin, P. Roy, P. E. Reimer, K. E. Mesick, *et al.*, Characterization of muon and electron beams in the Paul Scherrer Institute PiM1 channel for the MUSE experiment, *Physical Review C* **105**, 10.1103/physrevc.105.055201 (2022).
- [5] T. Rostomyan, E. Cline, I. Lavruchin, *et al.*, Timing detectors with SiPM read-out for the MUSE experiment at PSI, *Nuclear Instruments and Methods in Physics Research Section A: Accelerators, Spectrometers, Detectors and Associated Equipment* **986**, 164801 (2021).
- [6] P. Roy, S. Corsetti, M. Dimond, M. Kim, L. Le Potier, W. Lorenzon, R. Raymond, H. Reid, N. Steinberg, N. Wuerfel, K. Deiters, W. Briscoe, A. Golossanov, and T. Rostomyan, A liquid hydrogen target for the MUSE experiment at psi, *Nuclear Instruments and Methods in Physics Research Section A: Accelerators, Spectrometers, Detectors and Associated Equipment* **949**, 162874 (2020).
- [7] A. V. Gramolin, V. S. Fadin, A. L. Feldman, R. E. Gerasimov, D. M. Nikolenko, I. A. Rachek, and D. K. Toporkov, A new event generator for the elastic scattering of charged leptons on protons, *Journal of Physics G: Nuclear and Particle Physics* **41**, 115001 (2014).
- [8] L. Li, S. Strauch, *et al.*, Instrumental uncertainties in radiative corrections for the MUSE experiment, *Eur. Phys. J. A* **60**, 8 (2024), [arXiv:2307.06417 \[hep-ex\]](https://arxiv.org/abs/2307.06417).
- [9] D. Eyl, Messung des Spintransfers in elastischer und quasielastischer Streuung polarisierter Elektronen in den Reaktionen $H(\vec{e}, e'\vec{p})$ und $D(\vec{e}, e'\vec{p})$, Ph.D. thesis, Johannes Gutenberg-Universität Mainz (1993), mainz, Univ., Diss., 1993.
- [10] R. L. Workman *et al.* (Particle Data Group), Review of Particle Physics, *PTEP* **2022**, 083C01 (2022).
- [11] C. Nestler, Calibration and test of a lead-glass calorimeter for the MUSE experiment (2023), unpublished Semester Thesis.
- [12] Mesytec GmbH & Co. KG. MCFD-16 16 channel CFD with fast amplifier and pattern processing, accessed: 8-18-2023.
- [13] M. Böhmer, G. Korcyl, J. M. Ludwig Maier, A. Neiser, M. Palka, M. Penschuck, P. Strzempek, M. Traxler, and C. Ugur, A users guide to the TRB3 and FPGA-TDC based platforms, accessed: 8-19-2023.
- [14] Mesytec GmbH & Co. KG. MQDC-32 fast 32 channel VME charge integrating ADC, accessed: 8-18-2023.
- [15] W. Lin, Testing lepton universality with ep and μp elastic scattering in the MUSE experiment, *Ph.D. thesis*, Rutgers, The State University of New Jersey (2024).
- [16] M. Tanabashi, K. Hagiwara, K. Hikasa, K. Nakamura, Y. Sumino, F. Takahashi, J. Tanaka, *et al.* (Particle Data Group), Review of particle physics, *Phys. Rev. D* **98**, 030001 (2018).